



Synergistic photothermal/photodynamic suppression of prostatic carcinoma by targeted biodegradable MnO₂ nanosheets

Dewang Zeng, Lei Wang, Lu Tian, Shili Zhao, Xianfeng Zhang & Hongyan Li

To cite this article: Dewang Zeng, Lei Wang, Lu Tian, Shili Zhao, Xianfeng Zhang & Hongyan Li (2019) Synergistic photothermal/photodynamic suppression of prostatic carcinoma by targeted biodegradable MnO₂ nanosheets, *Drug Delivery*, 26:1, 661-672, DOI: [10.1080/10717544.2019.1631409](https://doi.org/10.1080/10717544.2019.1631409)

To link to this article: <https://doi.org/10.1080/10717544.2019.1631409>



© 2019 The Author(s). Published by Informa UK Limited, trading as Taylor & Francis Group.



[View supplementary material](#)



Published online: 01 Jul 2019.



[Submit your article to this journal](#)



Article views: 169



[View Crossmark data](#)

Synergistic photothermal/photodynamic suppression of prostatic carcinoma by targeted biodegradable MnO₂ nanosheets

Dewang Zeng^{a*}, Lei Wang^{b*}, Lu Tian^a, Shili Zhao^a, Xianfeng Zhang^c and Hongyan Li^a

^aDepartment of Nephrology, Huadu District People's Hospital of Guangzhou, Southern Medical University, Guangzhou, China; ^bGuizhou Population and Family Planning Science Research and Technology Guidance Institute, Guiyang, China; ^cDepartment of Gastroenterology, Huadu District People's Hospital of Guangzhou, Southern Medical University, Guangzhou, China

ABSTRACT

The biodegradability and clearance of metal-based nanomaterials have been questioned worldwide, which have greatly limited their clinical translation. Herein, ultrathin manganese dioxide (MnO₂) nanosheets with broad near-infrared (NIR) absorption and pH-dependent degradation properties were prepared. After being modified with polyethylene glycol-cyclic arginine-glycineaspartic acid tripeptide (PEG-cRGD), the MnO₂ nanosheets were then used as photothermal agent and nanocarrier to encapsulate chlorin e6 (Ce6) for targeted photothermal (PTT) and photodynamic (PDT) of cancer. As expected, the MnO₂-PEG-cRGD nanosheets show high Ce6 loading capacity (351 mg/g), superb photothermal conversion performance (37.2%) and excellent colloidal stability. These nanosheets also exhibit pH-dependent and NIR-induced Ce6 release. Furthermore, the MnO₂ nanosheets can be degraded by reacting with hydrogen peroxide in the acidic microenvironment, which are able to elevate the oxygen concentration *in situ* and thus reverses the tumor hypoxia. Thanks to these favorable properties and the cRGD-mediated tumor-targeted ability, the fabricated MnO₂-PEG-cRGD/Ce6 nanocomposites can be effectively up taken by alpha-v beta-3 ($\alpha_v\beta_3$) integrin over-expressed prostatic carcinoma PC3 cells and achieve favorable therapeutic outcomes under a single 660 nm NIR laser, which is also verified by *in vitro* studies. The biodegradable MnO₂-PEG-cRGD/Ce6 nanosheets developed in this work can be a promising nanoplatform for synergetic PTT/PDT cancer therapy.

ARTICLE HISTORY

Received 8 May 2019
Revised 9 June 2019
Accepted 9 June 2019

KEYWORDS



MnO₂ nanosheet; targeted delivery; photothermal therapy; photodynamic therapy; Ce6

Introduction


Cancer is a major worldwide menace to human health, which has become one of the main focuses of the biomedical world. The conventional cancer treatment methods, such as surgery, chemotherapy, and radiotherapy are often associated with lethal side effects, multidrug resistance, and low therapy efficiency (Huo et al., 2017; Shi et al., 2017; Bray et al., 2018). Great progress of nanoscience and nanobiotechnology has led to the generation of abundant antitumor therapy strategies (Fan et al., 2017; Tang et al., 2017). Among of various treatment strategies, phototherapy, including photothermal therapy (PTT; Jaque et al., 2014) and photodynamic therapy (PDT; Lucky et al., 2015) have drawn considerable attention due to the low systemic toxicity, high minimal invasiveness, and high selectivity. However, the conventional sole-modal therapy, either PTT or PDT, generally cannot restrain the tumors completely owing to the intrinsic drawbacks of phototherapy. Such as the insufficient penetration depth of near-infrared (NIR) light and inevitable injury to nearby normal tissues induced by high temperature in PTT,

as well as the local hypoxia of tumors severely hampers the application of PDT (Ocoy et al., 2016; Yang et al., 2016).

Synergistic therapy is one of promising ways that integrated two or more therapeutic modes into a single nanoplatform, which can enhance the treatment efficacy. Based on this, many researches have gradually shifted from PTT or PDT toward the combined PTT/PDT therapy, which results in remarkable super additive therapeutic effects (Dai et al., 2017; Fan et al., 2017). To fabricate this kind of combined therapy nanoplatform, well-designed nanoscale structures with multiple integrated functionalities, including photothermal conversion agent and photosensitizers are indispensable (Wu et al., 2018a; Zhang et al., 2011). However, different wavelengths of lasers were employed in most of strategies to activate the photothermal conversion agent and photosensitizer for PTT and PDT (Liu et al., 2014; 2017a), which is inconvenient due to the equipment/time cost and synergistic interactions evaluation. Thus, it is highly desirable to develop a photo-activatable nanoplatform to realize PTT and PDT simultaneously upon a single laser irradiation to avoid the time interval between PDT and PTT.

CONTACT Hongyan Li  lhyne1980@163.com  Department of Nephrology, Huadu District People's Hospital of Guangzhou, Southern Medical University, Guangzhou 510800, China

*These authors contributed equally to this work.

 Supplemental data for this article can be accessed [here](#).

© 2019 The Author(s). Published by Informa UK Limited, trading as Taylor & Francis Group.

This is an Open Access article distributed under the terms of the Creative Commons Attribution-NonCommercial License (<http://creativecommons.org/licenses/by-nc/4.0/>), which permits unrestricted non-commercial use, distribution, and reproduction in any medium, provided the original work is properly cited.

Recently, various types of nanocarriers, including graphene (Chen et al., 2016b), transition metal dichalcogenides (Li et al., 2015), black phosphorus (BP; Chen et al., 2017b), and other types (Song et al., 2015; Liu et al., 2018a; Zhen et al., 2018) were used for the combination of photothermal and photodynamic therapy to acquire the satisfactory synergistic therapeutic output. Two dimensional (2D) materials with a nanoscale thickness have been widely investigated in many fields (Liu et al., 2017b; Zhang et al., 2019). As a promising 2D nanomaterial, manganese dioxide (MnO_2) nanosheets have been preliminarily demonstrated in nanomedicine, especially in drug delivery because of its large surface areas, high NIR absorbance and good biocompatibility (Chen et al., 2016a). Compared with spherical nanoparticles, 2D MnO_2 nanosheets possess peculiar photothermal-conversion capability due to their ultrathin thickness intrinsically (Liu et al., 2018b), which can be served as an excellent photothermal agent for highly efficient PTT against tumor. Similar with other reported 2D nanomaterial, the large surface-area-to-volume ratio make the MnO_2 nanosheet can be used as drug delivery platforms to load various drug molecules via π - π stacking and hydrophobic interactions (Ji et al., 2018; Peng et al., 2018). Meanwhile, either in the form of spherical nanoparticles or 2D nanosheets, MnO_2 has been explored to overcome hypoxia because of the performance of acidic hydrogen peroxide (H_2O_2) response, thus results in improving the efficacy of PDT (Chen et al., 2019). What is more, manganese is a vital element in the human body and its metabolism will not cause serious immune responses. For instance, Chen et al. (2014) reported an intelligent theranostic platform based on 2D MnO_2 nanosheets for concurrent ultrasensitive pH-responsive MRI and drug release/delivery. Recently, ultrathin MnO_2 nanosheets-based theranostics nanoplatform has been designed by Liu et al. (2018b) for PTT of cancer. Despite these progresses of MnO_2 -based materials in nanomedicine applications, as yet, no synergistic PTT/PDT nanoplatform based on targeted modification MnO_2 nanosheets and photosensitizers has been reported. It is supposed that combining targeted modification MnO_2 nanosheets with photosensitizers should be a promising strategy for cancer treatment.

Herein, we have designed a nanoplatform by immobilizing chlorin e6 (Ce6) on polyethylene glycol-cyclic arginine-glycineaspartic acid tripeptide (PEG-cRGD) functionalized MnO_2 nanosheets (MnO_2 -PEG-cRGD/Ce6), which can be used for overcoming the hypoxia of cancer cells and synergistic PTT/PDT (Scheme 1). MnO_2 nanosheets were prepared by ultrasonically exfoliation of bulk MnO_2 , which was initially synthesized based on the oxidation of manganese chloride by H_2O_2 in the presence of tetramethylammonium hydroxide and then functionalized with PEG-cRGD to enhance their biocompatibility. The extraordinary surface area of MnO_2 nanosheets enables it highly efficient loading of small molecules to achieve different functions. Ce6, a widely used commercial photosensitizer was loaded on the surface of MnO_2 -PEG-cRGD. As expected, MnO_2 -PEG-cRGD nanosheets shows a high Ce6 loading capacity (351 mg/g) and exhibits pH/NIR responsive DOX release behavior, as well as significantly

increase of large singlet oxygen (SO) generation. Interestingly, the fabricated MnO_2 -PEG-cRGD/Ce6 exhibits superior photothermal conversion efficiency (37.2%), compared with MnO_2 -PEG-cRGD (21.4%). Owing to the modification of cRGD peptide, MnO_2 -PEG-cRGD/Ce6 could be specifically taken by alpha-v beta-3 ($\alpha_v\beta_3$) integrin receptors over-expressed prostatic carcinoma PC3 cells (Tian et al., 2019). This nanoplatform demonstrates a combination therapy including PTT and PDT based on *in vitro* tests, which exhibits an excellent synergistic anticancer activity under a single 660 nm NIR laser. Overall, our MnO_2 -PEG-cRGD/Ce6 is a promising biodegradable nanoplatform for synergistic PTT/PDT under a single laser and this work may explore the application of MnO_2 -based nanomaterials in combinatorial cancer therapy.

Materials and methods

Materials

Manganese chloride (MnCl_2), tetrabutylammonium hydroxide ($(\text{C}_4\text{H}_9)_4\text{NOH}$), calcein acetoxymethyl ester (calcein AM), and propidium iodide (PI) were purchased from Aladdin Reagent (Shanghai, China). Ce6 was obtained from J&K Scientific Ltd., Shanghai, China. 1,3-diphenylisobenzofuran (DPBF), $[\text{Ru}(\text{dpp})_3]\text{Cl}_2$ (RDPP), and 2,7-dichlorofluorescein diacetate (DCFH-DA) were obtained from Sigma-Aldrich (St. Louis, MO). **cRGD-PEG2000-NH₂ was bought from Xi'an Ruixi Biological Technology Co. Ltd (Xi'an, China).** Phosphate buffered solution (PBS), fetal bovine serum (FBS), penicillin-streptomycin, and dimethyl sulfoxide (DMSO) solution were purchased from Gibco Laboratories (Carlsbad, CA). 3-(4,5-dimethylthiazol-2-yl)-2,5-diphenyltetrazolium bromide (MTT), Annexin V-FITC/PI apoptosis and necrosis detection kit, and 4-6-diamidino-2-phenylindole (DAPI) were purchased from Yunnan Chenglv Biological Technology Co. Ltd (Kunming, Yunnan). The PC3 prostatic carcinoma cell line and L929 cell line maintained in Dulbecco's modified eagle medium (DMEM) medium was purchased from the Type Culture Collection of the Chinese Academy of Sciences (Shanghai, China). Deionized water (H_2O) was purified by a Millipore system (Milli-Q, 18.2 M Ω cm). All chemicals were used throughout.

Synthesis of MnO_2 -PEG-cRGD nanosheets

The MnO_2 nanosheets were synthesized according to the previous report with some modification (Zhao et al., 2014). In brief, a mixture of tetramethylammonium hydroxide (0.6 M, 15 mL) and 3 wt % H_2O_2 was added into MnCl_2 solution (0.3 M, 10 mL) within 15 s. The resulting dark brown suspension was stirred vigorously for 12 h at room temperature and the bulk manganese dioxide was obtained by centrifugation (2000 rpm, 10 min), washed thoroughly with water and ethanol for three times, and finally dried under vacuum at 55 °C. Then, MnO_2 nanosheets were prepared by ultrasonically exfoliation of the above bulk MnO_2 . Briefly, 10 mg of bulk manganese dioxide was dispersed in 20 mL water and ultrasonicated for 15 h (500 W). Then, the dispersion was

centrifuged at 2000 rpm for 20 min, and the supernatant was collected for further use. For cRGD-PEG2000-NH₂ modification, the cRGD-PEG2000-NH₂ (0.45 mg/mL, 15 mL) was added into a concentration of 4 mg mL⁻¹ MnO₂ nanosheets aqueous solution. After that, the mixture was ultrasonicated for 2 h and then centrifuged at 8000 rpm for 10 min. The precipitate was suspended in water for further use.

Synthesis of MnO₂-PEG-cRGD/Ce6 nanoparticles

For Ce6 loading, 0.5 mL of Ce6 (5 mg mL⁻¹ in DMSO) was dropwise added into 5 mL MnO₂-PEG-cRGD phosphate buffer solution (0.4 mg mL⁻¹, pH 7.4) and dispersed with the assistance of an ultrasonic bath. After stirring for 24 h in the dark, the resulting MnO₂-PEG-cRGD/Ce6 were collected by centrifugation and washed for three times with PBS to remove excess unbound Ce6. The whole process was carried out in the dark to avoid the quenching of Ce6. Meanwhile, the loading capacity can be calculated by using ultraviolet-visible (UV-Vis) spectrometer at a wavelength of 404 nm according to the previous report (Zhang et al., 2019).

Characterization

Transmission electron microscopy (TEM) was carried out by JEOL 2010 F electron microscope (Tokyo, Japan) at an operating voltage of 200 kV. X-ray diffraction (XRD) measurements were carried out using a D/max 2550 VB+/PC X-ray diffractometer (Rigaku Cop., Tokyo, Japan) with Cu K α radiation ($\lambda = 0.154056$ nm) at 40 kV. Dynamic light scattering (DLS) and zeta potential measurements were determined on Malvern Zetasizer (Nano ZS model ZEN3600, Worcestershire, UK). X-ray photoelectron spectroscopy (XPS) analysis was taken on an ESCALAB 250 spectrometer (Thermo-VG Scientific, Waltham, MA). Fourier-transform infrared spectroscopy (FTIR) spectra were obtained from a Nicolet Nexus 870 spectrometer (Nicolet Instruments Inc, USA). UV-Vis spectra were recorded on a UV3600 instrument (Shimadzu Corporation, Japan). Mn concentrations of samples were determined by inductively coupled plasma atomic emission spectrometer (ICP-AES, Agilent Technologies, Palo Alto, CA). NIR laser was acquired on a 660 nm laser device (Shanghai Connect Fiber Optics Company) and the temperature was recorded on a DT-8891E thermocouple linked to a digital thermometer (Shenzhen Everbest Machinery Industry, Shenzhen, China). Confocal laser fluorescence scanning images were obtained by Leica TCS SP2 microscope (CLSM, Leica Microsystems, Mannheim, Germany).

Photothermal property of the MnO₂-PEG-cRGD/Ce6

To study the photothermal conversion property of the MnO₂-PEG-cRGD/Ce6, different concentrations of dispersion (20, 50, 100, 150, and 200 μ g mL⁻¹) were placed in a quartz cuvette and irradiated with a 660 nm NIR laser (0.6 W/cm²) for 10 min and the temperature was recorded. Then, the MnO₂-PEG-cRGD/Ce6 solution at a concentration of 100 μ g/mL was irradiated with different power densities (0.2, 0.4,

0.6, 0.8, and 1.0 W/cm⁻²) over a period of 10 min. Meanwhile, the sample of water, MnO₂-PEG-cRGD and Ce6 were also tested for comparison. The photothermal stability of the MnO₂-PEG-cRGD/Ce6 was evaluated via monitoring the temperature change with or without 660 nm NIR laser irradiation (0.6 W/cm²) for five cycles. Finally, the photothermal conversion efficiency (η) of the MnO₂-PEG-cRGD/Ce6 and MnO₂-PEG-cRGD was calculated by the following equation that was reported by Wu et al. (2018b).

$$\eta = \frac{hS(T_{\max} - T_{\text{am}}) - Q_0}{I(1 - 10^{-A})} \quad (1)$$

Where, h is the heat transfer coefficient, S is the surface area of the container, T_{\max} is equilibrium temperature, T_{am} is surrounding ambient temperature, Q_0 is the heat associated with the light absorbance of the solvent, I is the laser power, and A is the absorbance of the MnO₂-PEG-cRGD/Ce6 or MnO₂-PEG-cRGD at 660 nm.

In vitro pH/NIR responsive Ce6 release

In vitro Ce6 release from MnO₂-PEG-cRGD/Ce6 was measured at varied pH of 7.4 and 5.5 with or without 660 nm laser irradiation. In brief, 10 mg of MnO₂-PEG-cRGD/Ce6 were dispersed in 5 mL of PBS solution (pH 7.4 or 5.0). Then, 1 mL of solution was taken and encapsulated into a dialysis bag (MWCO: 5000 Da) and dialyzed against PBS. Afterward, the sample was directly irradiated by 660 nm NIR laser (0.6 W/cm²) for 10 min. At designated time intervals, 1.5 mL of solution outside the dialysis bag was collected and the amount of released Ce6 was determined with UV-Vis spectrometer at a wavelength of 404 nm.

Photodynamic properties of the MnO₂-PEG-cRGD/Ce6

The production of oxygen (O₂) was detected with RDPP, whose fluorescence can be quenched by O₂ (Ma et al., 2017). In brief, 100 μ L of ethanol solution of RDPP (10 \times 10⁻³ M) was added to MnO₂-PEG-cRGD/Ce6 (1 mL, 50 μ g mL⁻¹). Then 300 μ L of H₂O₂ (100 mM) was added and the fluorescence intensity of RDPP ($\lambda_{\text{ex}} = 455$ nm) at 615 nm was recorded every 2 min. Meanwhile, the H₂O₂ or MnO₂-PEG-cRGD/Ce6 without H₂O₂ addition was also tested as control.

Next, the generation of SO (¹O₂) was evaluated by the chemical probe DPBF. Typically, DPBF ethanol solution (20 μ L, 100 mM) were added to 1 mL of free Ce6 or MnO₂-PEG-cRGD/Ce6 solution. Then, 100 mM of H₂O₂ was added into the above system, following by laser irradiation (660 nm, 0.6 W/cm²) for 10 min. The absorption intensity of DPBF at 410 nm was monitored. Meanwhile, the sample without laser irradiation was used as control.

Degradation behavior of MnO₂-PEG-cRGD

The degradation behavior of as-prepared MnO₂-PEG-cRGD was investigated according a previous report (Chen et al., 2017a,b). MnO₂-PEG-cRGD (1.5 mg) was dispersed in 30 mL of PBS solution (pH 5.0) with addition of H₂O₂ (10 mM) and

maintained at 37 °C shaker with shaking speed of 100 rpm. At different time points, 1 mL of solution was taken out and centrifuged, then were re-dispersed by ethanol and dropped on copper grid for TEM observation.

Cell culture and biocompatibility of MnO₂-PEG-cRGD in vitro

PC3 cells and L929 cells were cultured in DMEM supplemented with 10% FBS and penicillin (100 units/mL)/streptomycin (100 µg/mL) under standard conditions (37 °C, 5% carbon-di-oxide). To estimate the biocompatibility of MnO₂-PEG-cRGD, PC3 cells and L929 cells (2×10^4 cells/well) were seeded in 96-well plates and then incubated for 24 h, respectively. After fully adhesion and spread of cells, the fresh medium containing different concentrations (200, 100, 50, 25, 12.5, and 6.25 µg/mL) of MnO₂-PEG-cRGD was added and cultured for another 24 h. Finally, the cells were repeatedly rinsed with PBS and the cell viability was evaluated by standard MTT assay.

Generation of intracellular SO

First, the intracellular generation of O₂ was investigated also with RDPP. HeLa cells (2.0×10^5 cells per dish) were seeded into culture dishes and incubated with RDPP (0.5 µM) for 4 h. After that, the cells were further incubated with MnO₂-PEG/Ce6, MnO₂-PEG-cRGD/Ce6 and free Ce6 with an equivalent Ce6 concentration of 10 µg mL⁻¹ for 24 h. The cells were washed with PBS for three times and then exposed to 1 mM H₂O₂ in DMEM medium for 45 min at 37 °C. Finally, the cells were washed with PBS and fluorescence images were captured by the CLSM. The RDPP were excited at 488 nm, and the emission was collected between 600 and 700 nm. The cells without any treatment served as control. Next, the intracellular ¹O₂ generation was detected by using the DCFH-DA probe. Briefly, PC3 cells (2×10^5 cells per dish) were treated with MnO₂-PEG-cRGD/Ce6 and free Ce6 with an equivalent Ce6 concentration of 10 µg mL⁻¹ overnight. After that, the cells were rinsed with PBS, followed by the addition of DCFH-DA (1 mL, 10 µM in DMEM medium) and incubated for 20 min. Then, the cells were irradiated with 660 nm light (0.6 W cm⁻²) for 10 min. The cells without any treatment were served as controls. The fluorescence images were captured by CLSM at an excitation of 488 nm.

In vitro cellular uptake

The targeted cell uptake of the MnO₂-PEG-cRGD/Ce6 was also investigated. PC3 cells (α_vβ₃ integrin receptor positive) were seeded on a glass-bottomed culture dish (2×10^5 cells/well) for 24 h. All the cells were treated with MnO₂-PEG/Ce6 and MnO₂-PEG-cRGD/Ce6 with or without 660 nm laser irradiation for 10 min at an equivalent Ce6 concentration of 5 µg mL⁻¹ for 4 h. After that, the cells in all the groups were washed three times with PBS, fixed with 4% formaldehyde for 20 min. The cell nuclei were stained with DAPI for 10 min, the cells were washed three times with PBS (5 mL) and then

imaged by a CLSM (Jena, Germany). For competitive inhibition experiments, PC3 cells were pretreated for 4 h with free cRGD (10 µM) prior to incubation with MnO₂-PEG-cRGD/Ce6. For bio-transmission electron microscope (Bio-TEM, Hitachi HT7700, Tokyo, Japan) analysis, a similar protocol was performed as the one used in CLSM experiment. After washing with PBS three times, PC3 cells were fixed with 2% glutaraldehyde for 2 h at room temperature, followed by 2 h in 1% OsO₄, dehydrated through a graded ethanol series, embedded in EPOM812 and examined by bio-TEM imaging.

To further confirm the cellular uptake of the MnO₂-PEG-cRGD/Ce6, ICP-AES analysis was performed. Similarly, PC3 and L929 cells were treated with free Ce6 and MnO₂-PEG-cRGD/Ce6 with or without 660 nm laser irradiation for 10 min at an equivalent Ce6 concentration of 5 µg mL⁻¹ for 4 h. Afterwards, the cells were washed with PBS for three times, trypsinized with 0.05% trypsin-EDTA, centrifuged, and resuspended in 1 mL of PBS. Subsequently, the cells were digested by aqua regia solution (1 mL) overnight, and diluted with 1 mL of water, followed by ICP-AES assay to determine the Mn content in the cell samples.

In vitro antitumor efficiency of MnO₂-PEG-cRGD/Ce6

To study the antitumor performance *in vitro*, PC3 cells were cultured in 96-well plates at a density of 1×10^4 cells per well and incubated for 24 h. Then, the medium was replaced with 100 µL of fresh medium containing different concentrations of MnO₂-PEG-cRGD, free Ce6, and MnO₂-PEG-cRGD/Ce6 at the equivalent Ce6 concentrations and the cells were incubated for 6 h. After that, the cells were irradiated by a 660 nm light (0.6 W cm⁻²) for 10 min. After incubation for another 10 h, the cell viability was evaluated by MTT assay. Meanwhile, the cytotoxicity of MnO₂-PEG/Ce6 at the equivalent Ce6 concentrations against PC3 cells was also measured for comparison.

To further prove the PTT/PDT therapy efficacy, live/dead cell staining assay was conducted. PC3 cells were seeded in six-well plates at a density of 5×10^5 cells per well for 24 h incubation, followed by incubation with MnO₂-PEG-cRGD, free Ce6, and MnO₂-PEG-cRGD/Ce6 at equivalent Ce6 concentrations of 5 µg mL⁻¹, respectively. After incubation for 6 h, the cells were exposed to 660 nm light (0.6 W cm⁻²) for 10 min. After that, the cells were stained with Calcein-AM (5 µg mL⁻¹) and PI (10 µg mL⁻¹) for 30 min at 37 °C. Then, the cells after different treatments were washed with PBS three times and monitored with an inverted fluorescence microscope. The untreated cells were used as the control. The synergistic effect of PTT/PDT was evaluated by combination index (CI) analysis (Xu et al., 2018). Consequently, CI > 1 denotes antagonism; CI = 1 additivity, and CI < 1 synergism.

Cell apoptosis assay

The apoptosis and necrosis assay of PC3 cells treated with MnO₂-PEG-cRGD under laser irradiation was evaluated by flow cytometry. The PC3 cells were seeded in six-well plate

at a density of 5×10^5 cells/well and cultured for 24 h. Then, the cells were treated separately with MnO_2 -PEG-cRGD, free Ce6 and MnO_2 -PEG-cRGD/Ce6 (the equivalent Ce6 concentrations of $5 \mu\text{g mL}^{-1}$). After 6 h incubation, the cells were irradiated with 10 min laser irradiation (0.6 W/cm^2). Cells untreated and subjected to only laser irradiation was tested as the control. After further incubation for 18 h, all the cells were digested, collected, and re-suspended in the annexin-binding buffer. After that, the cells were stained with recombinant human anti-Annexin-V-FITC ($5 \mu\text{L}$) and PI ($5 \mu\text{L}$) for 15 min in the dark, and then examined by flow cytometry (BD FACS Aria TM III, BD Biosciences, Franklin Lakes, NJ).

Statistical analysis

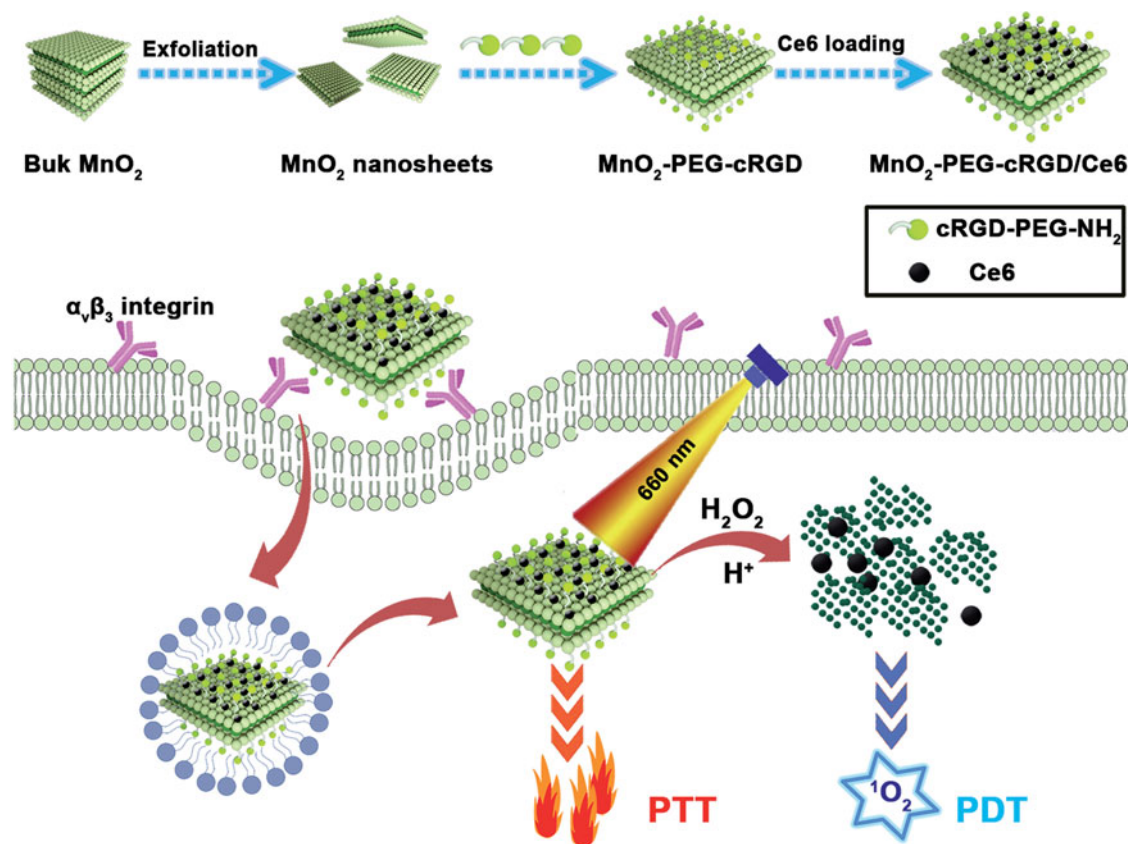
One-way analysis of variance (ANOVA) statistical method was performed to evaluate the experimental data. A value of 0.05 was selected as the significance level and the data were indicated with (*) for $p < .05$, (**) for $p < .01$, and (***) for $p < .001$, respectively.

Results and discussion

Preparation and characterization of MnO_2 -PEG-cRGD/Ce6 nanoparticles

MnO_2 nanosheets were prepared from bulk MnO_2 , which is synthesized by oxidation of MnCl_2 in the presence of H_2O_2

and tetramethylammonium hydroxide (Zhao et al., 2014). Then, as-prepared MnO_2 nanosheets were modified with cRGD-PEG2000- NH_2 under vigorous sonication for compatible with biological application as well as introduce the targeting ligands (Scheme 1). As revealed by TEM imaging, the as-synthesized MnO_2 -PEG-cRGD nanosheets exhibited the obvious planar morphology with the thickness of about 1 nm, indicating the few layers structure (Figure 1(B)). Compared to MnO_2 nanosheets (Figure 1(A)), the PEG and cRGD modification showed negligible change of morphology and uniform layer structure. DLS results show that the average diameter of MnO_2 and MnO_2 -PEG-cRGD are 217 ± 14.6 and 271 ± 26.7 nm, respectively (Figure 1(C)). XRD spectra of MnO_2 -PEG-cRGD (Supplementary Figure S1) showed the obvious characteristic peaks at $2\theta = 36.6$ and 65.9° , which are corresponded to (221) and (002) planes of $\alpha(\text{m})\text{-MnO}_2$ (Devaraj & Munichandraiah, 2008), indicated the formation of 2D-layered MnO_2 nanosheets. Also, the valence states of manganese component were determined by XPS analysis (Supplementary Figure S2). It can be observed that two peaks at 653.5 and 642.7 eV from high-resolution XPS spectra (Figure 1(D)) of Mn 2p associated with the Mn 2p_{1/2} and Mn 2p_{3/2} peaks of MnO_2 , respectively (Wu et al., 2018c). The FTIR spectrum of the MnO_2 -PEG-cRGD shows the strong bands of amide I and amide II around 1652 and 1524 cm^{-1} and the characteristic peaks of PEG (944 , 1358 , and 2972 cm^{-1}), confirming the successful modification of PEG-cRGD on the surface of MnO_2 nanosheets (Supplementary



Scheme 1. Schematic illustration for the preparation of MnO_2 -PEG-cRGD/Ce6 composite as a biodegradable nanoplatform for synergistic PTT/PDT targeted therapy.

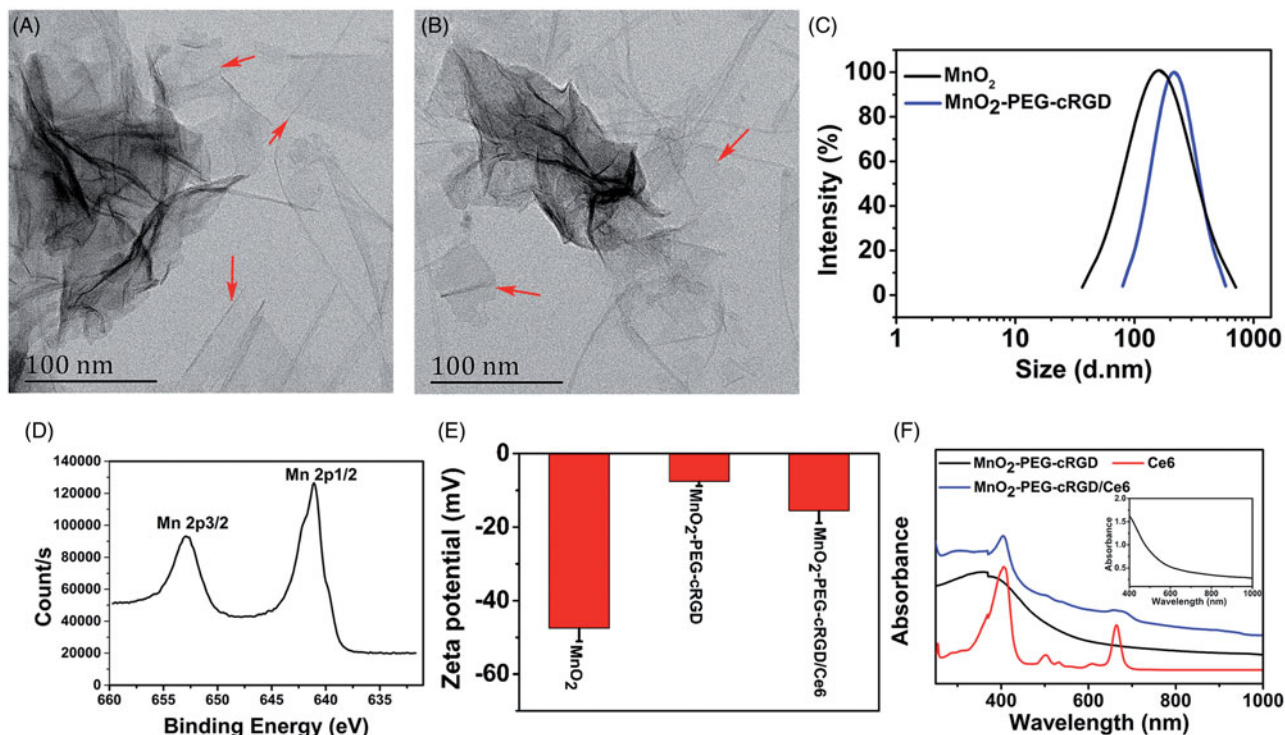


Figure 1. TEM images of (A) MnO_2 and (B) MnO_2 -PEG-cRGD nanosheets. (C) DLS size distribution of MnO_2 and MnO_2 -PEG-cRGD nanosheets. (D) Mn 2p XPS spectra for MnO_2 nanosheets. (E) Zeta potential of MnO_2 , MnO_2 -PEG-cRGD, and MnO_2 -PEG-cRGD/Ce6 ($n = 3$). (F) UV-Vis spectra of Ce6, MnO_2 -PEG-cRGD, and MnO_2 -PEG-cRGD/Ce6. Inset: UV-Vis spectra of MnO_2 -PEG-cRGD nanosheets between 400 and 1000 nm.

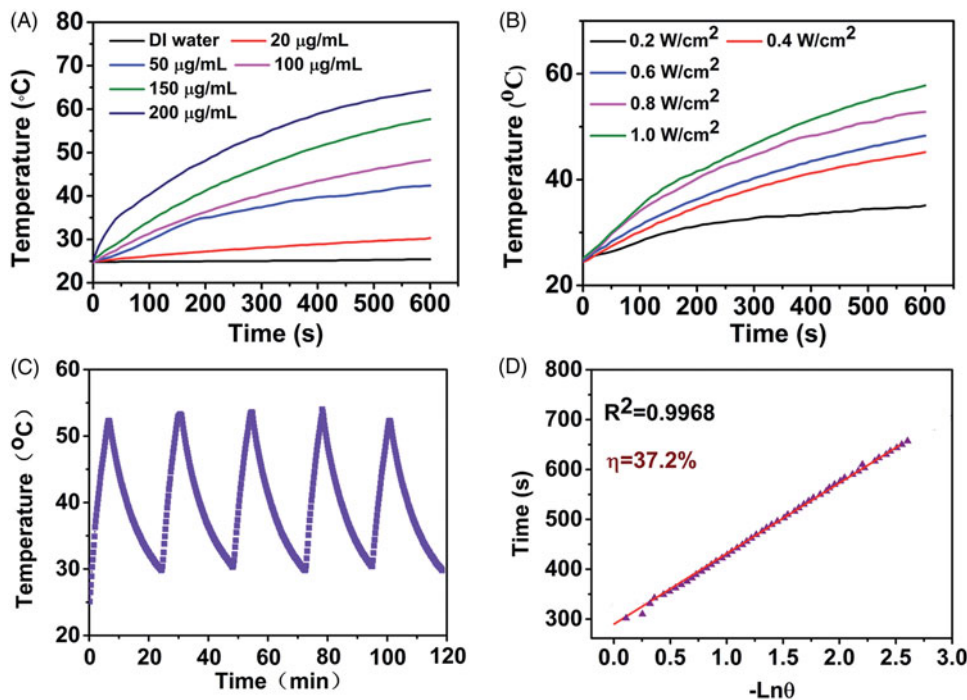


Figure 2. (A) Photothermal conversion curves of water and MnO_2 -PEG-cRGD/Ce6 nanoparticles at different concentrations upon irradiation with an 660 nm laser (0.6 W cm^{-2}). (B) Photothermal conversion curves of MnO_2 -PEG-cRGD/Ce6 nanoparticles ($100 \mu\text{g mL}^{-1}$) at different laser power densities. (C) Photothermal conversion stability of MnO_2 -PEG-cRGD/Ce6 nanoparticles. The laser was turned on for 10 min and then turned off for each cycle. (D) Linear relationship between time and $-\ln \theta$ calculated from cooling period after the laser was turned off.

Figure S3). Also, the zeta potentials of MnO_2 nanosheets are around -47.5 mV but turned into -7.6 mV after the formation of MnO_2 -PEG-cRGD (Figure 2(E)). Meanwhile, MnO_2 -PEG-cRGD exhibits good dispersity in PBS, but the MnO_2 nanosheets showed lower colloidal stability (Supplementary

Figure S4), thus confirming the PEGylation could improve the physiological stability of nanomaterials.

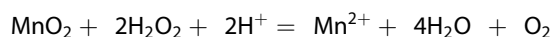
Similar with some other 2D materials, the two-dimensional structure of MnO_2 -PEG-cRGD nanosheets could be used as nanocarrier to load some small molecules with

excellent loading capacity. Ce6 is a widely used photosensitizer with NIR light absorption, which is able to generate cytotoxic singlet oxygen for PDT (Dong et al., 2016). Herein, Ce6 was loaded on the surface of MnO₂-PEG-cRGD nanosheet to form MnO₂-PEG-cRGD/Ce6 nanosystem via physical adsorption. The decreased zeta potential of MnO₂-PEG-cRGD/Ce6 also suggested that the Ce6 was successfully loaded onto MnO₂-PEG-cRGD (Figure 1(E)). Compared to MnO₂-PEG-cRGD, two new absorption peaks at 407 and 665 nm was appeared in the UV-Vis-NIR spectra of MnO₂-PEG-cRGD/Ce6 (Figure 1(F)), which was assigned to characteristic Soret-band and Q-band of Ce6, thus indicating the successful loading of Ce6. At the studied conditions, about 351 mg of Ce6 was loaded into 1 g of MnO₂-PEG-cRGD. The high drug loading capacity may be due to the Mn atoms in the sheets could form special coordinate bonds with the Mn atoms in Ce6 molecules (Ma et al., 2018).

Photothermal and photodynamic properties of MnO₂-PEG-cRGD/Ce6

Inspired by the strong NIR absorbance of MnO₂-PEG-cRGD/Ce6, the photothermal conversion property of the nanosheets was explored. It should be noted that 660 nm laser was employed as the light source to realize PTT and PDT simultaneously upon a single laser irradiation to avoid the time interval in biomedical application. As shown in Figure 2(A,B), the temperature of the MnO₂-PEG-cRGD/Ce6 nanoparticles increased sharply under 660 nm NIR irradiation. The temperature of the MnO₂-PEG-cRGD/Ce6 solution (100 µg/mL) increased to 64.4 °C after 10 min of laser (1 W/cm²) irradiation, while the temperature of deionized water only increased by 0.7 °C. Meanwhile, both concentration and laser-power-dependent photothermal effect was observed, indicated the heat generation could be neatly tuned. Meanwhile, MnO₂-PEG-cRGD/Ce6 showed an excellent yet stable light-to-heat conversion property within five cycles of laser irradiation (Figure 2(C)). On the basis of the data obtained from the time constant of heat transfer and the maximum steady-state temperature (Figure 2(D) and Supplementary Figure S5), the photothermal conversion efficiency (η) of MnO₂-PEG-cRGD/Ce6 was assessed to be 37.2%, which is higher than that of MnO₂-PEG-cRGD (21.4%) as well as higher than some literature reported 2D PTT agents (Yang et al., 2017b). The enhanced photothermal conversion efficiency confirmed the excellent photothermal synergistic effect of MnO₂-PEG-cRGD and Ce6, which provides a potential for photothermal therapy.

It is known that MnO₂ is reduced into Mn(II) ions in presence of acidic H₂O₂ by oxidation of H₂O₂ into O₂, which could be explained by the following reactions (Chen et al., 2016a):



Considering about this reactivity, we wondered whether the reduction of MnO₂ would induce the dissociation of MnO₂-PEG-cRGD/Ce6. Thus, the degradation behavior of MnO₂-PEG-cRGD/Ce6 nanoparticles in acidic H₂O₂ was

carefully studied. The morphology evolution of MnO₂-PEG-cRGD/Ce6 in the process of degradation was directly observed using TEM (Figure 3(A)). After only 10 min of immersion in PBS (pH 5) containing 1 mM of H₂O₂, degradation is evident as certified by the change of shape and more distinct structure collapse. After 30 min, the MnO₂-PEG-cRGD/Ce6 with undergone destructive change was observed and eventually become ultra-small and irregularly ruptured clusters after 1 h incubation. Due to the cancer cell is often featured with high H₂O₂ levels and low pH values, the biodegradability of this nanosheets would favor its application for cancer therapy.

Then, the oxygen generation of MnO₂-PEG-cRGD/Ce6 was then quantified by using an RDPP O₂ probe. Obviously, the fluorescence intensity of RDPP is quenched rapidly after addition of H₂O₂ (100 µM) to MnO₂-PEG-cRGD/Ce6 PBS suspension (pH 5) within 4 min (Figure 3(B)), whereas much slower quenching of RDPP was occurred in pH 7.4. By contrast, there is no fluorescence intensity decreased was observed in the group of Ce6 or MnO₂-PEG-cRGD/Ce6 without H₂O₂. These results confirmed that the generation of O₂ is resulted from the oxidation of H₂O₂ by MnO₂ nanosheets. Next, we wondered whether MnO₂-PEG-cRGD/Ce6 in the presence of H₂O₂ could be used for PDT or not. Thus, the production of ¹O₂ by MnO₂-PEG-cRGD/Ce6 under laser irradiation (660 nm, 0.6 W/cm²) was measured by a DPBF probe. As expected, the absorption of DPBF was decreased in MnO₂-PEG-cRGD/Ce6 suspension, and more obvious decrease of the absorbance of DPBF was detected in the presence of H₂O₂, which is due to the H₂O₂-triggered O₂ production (Figure 3(C)). As compared to the free Ce6, the absorbance intensity of DPBF gradually decreases with a relative slow rate in MnO₂-PEG-cRGD/Ce6, indicating the photodynamic effect of MnO₂-PEG-cRGD/Ce6 deriving from the slow release of Ce6. These results demonstrated the MnO₂-PEG-cRGD/Ce6 nanoparticles could be served as an efficient PDT agent to reverse the tumor hypoxia for enhancing the therapeutic efficiency under specific laser irradiation.

In vitro pH/NIR responsive Ce6 release

Previous studies have been reported that most of 2D materials-based nanoplatfrom can release the loaded cargos in response to acidic and thermal stimuli (Karimi et al., 2016). Thus, the feasibility of pH and light irradiation-triggered release of Ce6 from the nanosystem was further investigated under different treatments. As illustrated in Figure 3(D), less than 8% of Ce6 was released from the MnO₂-PEG-cRGD/Ce6 at pH 7.4 after 24 h, while for pH 5, the amount of Ce6 released reached to around 25.2% within 24 h. The pH-responsive release of Ce6 may be due to the protonation of amino groups in Ce6 under acidic conditions, resulting in increasing the hydrophilicity of Ce6 and decreasing binding with nanosheets. In addition, the release performance triggered by NIR laser irradiation was further investigated. As shown in Figure 3(D), a significantly increased Ce6 release was obtained: 43.6% at pH = 7.4 and 73.5% at pH = 5 under 660 nm laser irradiation for 5 min time interval. The NIR-

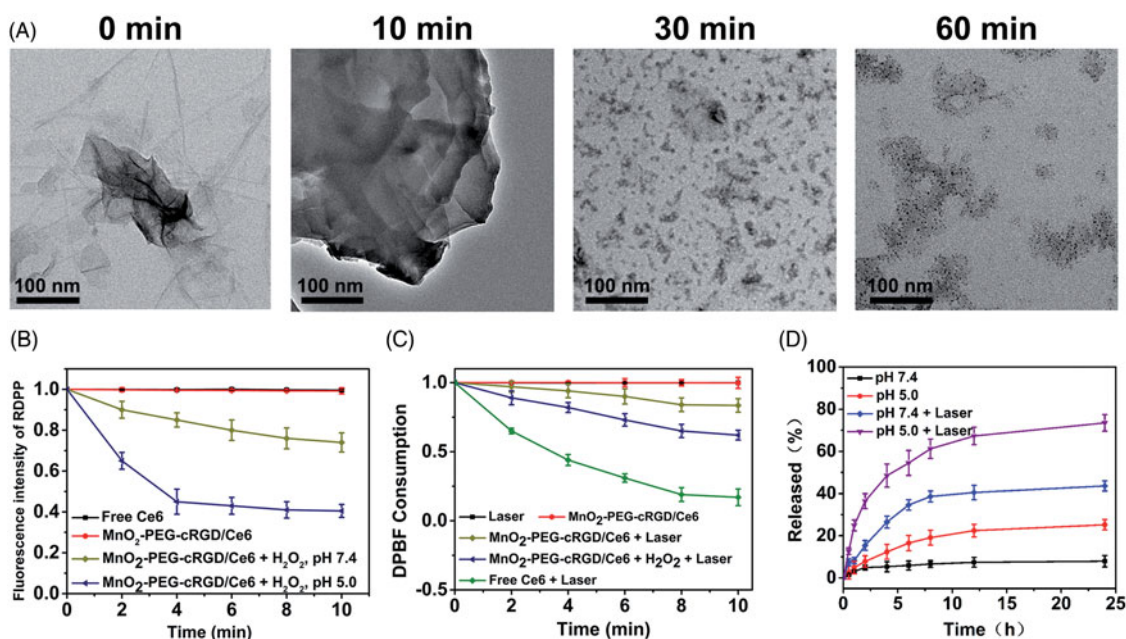


Figure 3. (A) TEM observation of MnO₂-PEG-cRGD/Ce6 after degradation in pH 5 containing 1 mM of H₂O₂ for 10, 30, and 60 min, respectively. (B) Generation of O₂ under the reduction of MnO₂-PEG-cRGD/Ce6 (50 μg mL⁻¹) by 10 × 10⁻³ M H₂O₂ in acidic PBS (pH 5). (C) Consumption of DPBF over time due to ¹O₂ generation: (a) laser only, (b) MnO₂-PEG-cRGD/Ce6 without laser, free Ce6, and (c) MnO₂-PEG-cRGD/Ce6 with laser in the absence (d) or presence (e) of 100 mM H₂O₂ (pH 7.4). (D) Release profiles of Ce6 at different pHs with or without 660 nm NIR laser (0.6 W/cm², 10 min).

induced drug release may be due to the MnO₂-PEG-cRGD/Ce6 could absorb the NIR light and convert into local heating, the heat dissociates the strong interactions between Ce6 and nanosheets, thus more Ce6 molecules are released (Lu et al., 2017).

In vitro biocompatibility and generation of intracellular singlet oxygen

Encouraged by the above-mentioned results, we further evaluated the *in vitro* biocompatibility and ¹O₂ generation efficiency of the nanoparticles. Biocompatibility of MnO₂-PEG-cRGD is the prerequisite for their biomedical application. Hence, the cytotoxicity of MnO₂-PEG-cRGD nanosheets was examined in PC3 cells and L929 cells by MTT assay (Figure 4(A)). No obvious cytotoxicity of MnO₂-PEG-cRGD in different cell lines was observed, even at concentrations up to 200 μg mL⁻¹, indicating their good biocompatibility for further biological applications.

Then, the intracellular O₂ generation ability of MnO₂-PEG-cRGD/Ce6 was examined by CLSM with O₂ probe RDPP. It can be observed that the green fluorescence gradually quenched in the cells after incubated with MnO₂-PEG/Ce6 or MnO₂-PEG-cRGD/Ce6, while strong RDPP fluorescence was still detected in the PC3 cells that treated with free Ce6 (Supplementary Figure S6). These results indicated the increase of intracellular O₂ resulted from the cleavage of intracellular H₂O₂ by MnO₂-PEG/Ce6 or MnO₂-PEG-cRGD/Ce6, which overcomes the hypoxia of cancer cells. Furthermore, according to the intensity of green fluorescence, O₂ generation was significantly high in the cells treated by MnO₂-PEG-cRGD/Ce6, which may be due to the high uptake of MnO₂-PEG-cRGD/Ce6. Next, the intracellular ¹O₂ production

by MnO₂-PEG-cRGD/Ce6 within PC3 cells was examined by using DCFH-DA probe. After treated with MnO₂-PEG-cRGD/Ce6 with 660 nm laser irradiation (0.6 W cm⁻²), strong fluorescence intensity of DCFH-DA was observed (Figure 4(B)), while much weaker DCFH-DA fluorescence in the cells treated with Ce6 and MnO₂-PEG-cRGD. These results confirmed MnO₂-PEG-cRGD/Ce6 can improve the production of ¹O₂ under laser irradiation, which can greatly improve the therapeutic effect of PDT.

In vitro cellular uptake

It has been recognized that cRGD-decorated nanoparticles could be more efficiently internalized by cells via α_vβ₃ integrin receptor mediated endocytosis (Fang et al., 2017; Zhong et al., 2014). Therefore, the cellular uptake behavior of our MnO₂-PEG-cRGD/Ce6 nanoparticles was investigated by using PC3 cells (α_vβ₃ integrin receptor positive). As shown in Figure 4(C), the PC3 cells group treated with MnO₂-PEG-cRGD/Ce6 showed greater Ce6 fluorescence than those treated with MnO₂-PEG/Ce6, which reflected the active targeting effect of MnO₂-PEG-cRGD/Ce6 toward PC3 cells. Also, the competitive inhibition experiments revealed that 4 h pre-treatment of PC3 cells with free cRGD before incubation with MnO₂-PEG-cRGD/Ce6 under NIR laser irradiation displayed weak Ce6 fluorescence, further proved active targeting effect of MnO₂-PEG-cRGD/Ce6 toward PC3 cells. In addition, the Ce6 signal was much stronger both in cytoplasm and nuclei after the NIR light irradiation (660 nm, 10 min), which is due to the local mild hyperthermia not only caused minor disruptions to cell membrane for improving intracellular delivery of nanoparticles (Lu et al., 2017), but also significantly promoted the Ce6 release.

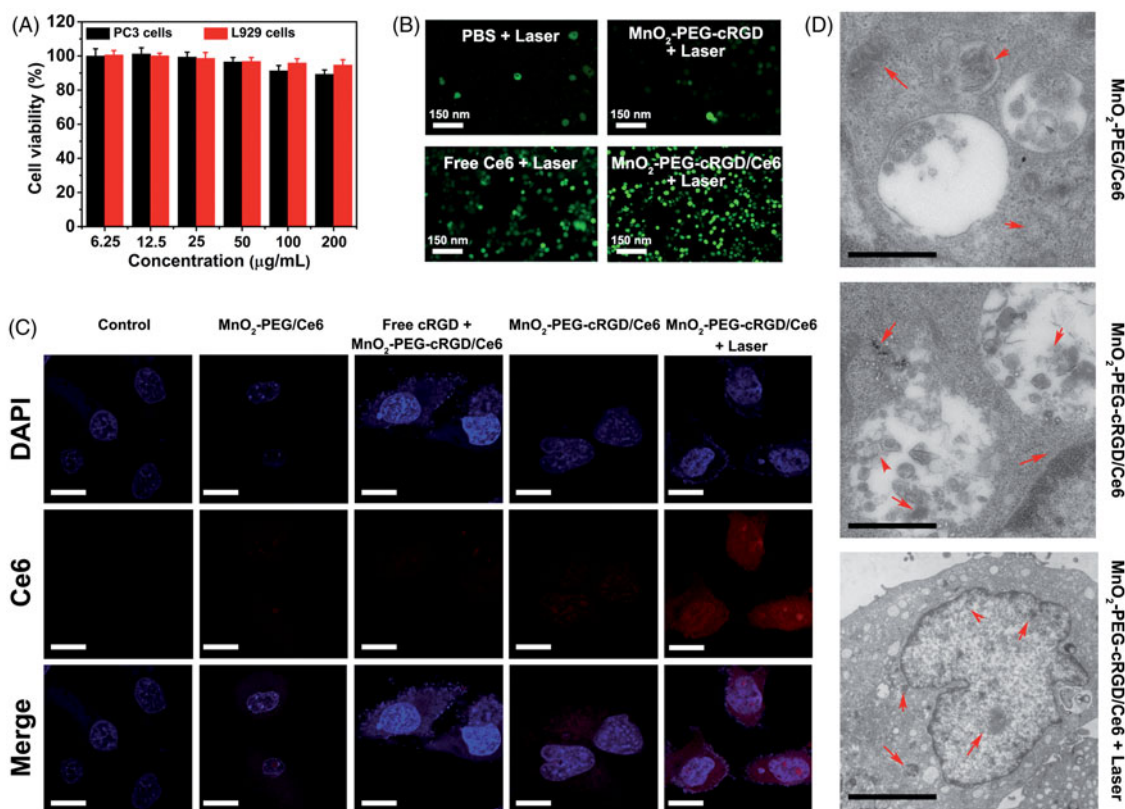


Figure 4. (A) Relative viability of PC3 and L929 cells after incubation with MnO₂-PEG-cRGD (25, 50, 100, 200, 300, and 500 μg mL⁻¹) for 24 h. (B) CLSM of intracellular ¹O₂ generation after PC3 cells were treated with PBS, MnO₂-PEG-cRGD, free Ce6, and MnO₂-PEG-cRGD/Ce6 under laser illumination. (C) CLSM of PC3 cells treated with MnO₂-PEG/Ce6 and MnO₂-PEG-cRGD/Ce6 (relative Ce6 = 5.0 μg/mL) for 4 h with or without laser illumination (Blue fluorescence is associated with DAPI; red fluorescence is expressed by released Ce6). Scale bars = 50 μm. (D) Bio-TEM images of PC3 cells incubated with MnO₂-PEG/Ce6 and MnO₂-PEG-cRGD/Ce6 with or without laser irradiation. Scale bar: 1 μm.

To check the targeting ability of MnO₂-PEG-cRGD/Ce6, the Mn uptake within PC3 cells or L929 cells that treated with the nanoparticles was further investigated by quantitative ICP-AES analysis (Supplementary Figure S7). Obviously, the uptake Mn in the PC3 cells is significantly higher than that in L929 cells owing to the targeting effect of cRGD. Also, the uptake of Mn in laser irradiation group was as higher as nearly three-fold than that for MnO₂-PEG-cRGD/Ce6 without laser irradiation. Meanwhile, the localization of the NPs has been evaluated by bio-TEM analysis. PC3 cancer cells were incubated with MnO₂-PEG-cRGD/Ce6 and MnO₂-PEG-cRGD/Ce6 and corresponding bio-TEM image is respectively displayed in Figure 4(D). Under TEM observation, a greater number MnO₂-PEG-cRGD/Ce6 nanoparticle were found in lysosomes in MnO₂-PEG-cRGD/Ce6 after NIR light irradiation. By contrast, fewer nanoparticles were endocytosed in the group that treated with MnO₂-PEG-cRGD/Ce6, as well as MnO₂-PEG/Ce6 nanoparticles. These results verified that MnO₂-PEG-cRGD/Ce6 mediate cellular uptake mostly due to the combination of receptor-mediated endocytosis and NIR-induce local mild hyperthermia.

In vitro synergistic therapy

Next, we detected the cytotoxicity of combinatorial PTT and PDT of MnO₂-PEG-cRGD/Ce6 nanoplatfor for cancer cells *in*

vitro. First, cells were incubated with free Ce6, MnO₂-PEG-cRGD, or MnO₂-PEG-cRGD/Ce6 in presence of NIR irradiation (660 nm, 0.6 W cm⁻²) for 10 min at increasing concentrations. Clearly, a MnO₂-PEG-cRGD or Ce6 dose-dependent cytotoxicity was observed in both treatments (Figure 5(A)). Ultimately, about 90% of the PC3 cells were killed by the MnO₂-PEG-cRGD/Ce6-induced synergistic effect (MnO₂-PEG-cRGD: 100 μg/mL, Ce6: 5 μg/mL), which is much higher than that of MnO₂-PEG-cRGD with 30% of cells death and free Ce6 with 34% of cells death. Meanwhile, cells treated with MnO₂-PEG/Ce6 also exhibited a dosage-dependent cell death (Figure S8), but a bit lower than that of treated with MnO₂-PEG-cRGD/Ce6 at the same concentration of Ce6, owing to the absence of cRGD modification. The half maximal inhibitory concentration (IC₅₀) of MnO₂-PEG-cRGD/Ce6 is 0.36 μg mL⁻¹, which is smaller than that of Ce6 (2.74 μg mL⁻¹) and MnO₂-PEG-cRGD/Ce6 (0.61 μg mL⁻¹). Overall, MnO₂-PEG-cRGD/Ce6 show the best therapeutic output compared with MnO₂-PEG-cRGD and MnO₂-PEG/Ce6, indicating the advantage of synergistic PTT/PDT cancer therapy. Also, the combination index (CI) of PTT and PDT is calculated to be 0.36, further verifying the synergistic effect. For deeper insight of the synergistic effect, live/dead cell staining assay was conducted (Figure 5(B)). Compared to the control group and any other treatment group, almost all of the cells were death after treated with MnO₂-PEG-cRGD/Ce6 with laser irradiation. These results are consistent with the results of MTT experiments.

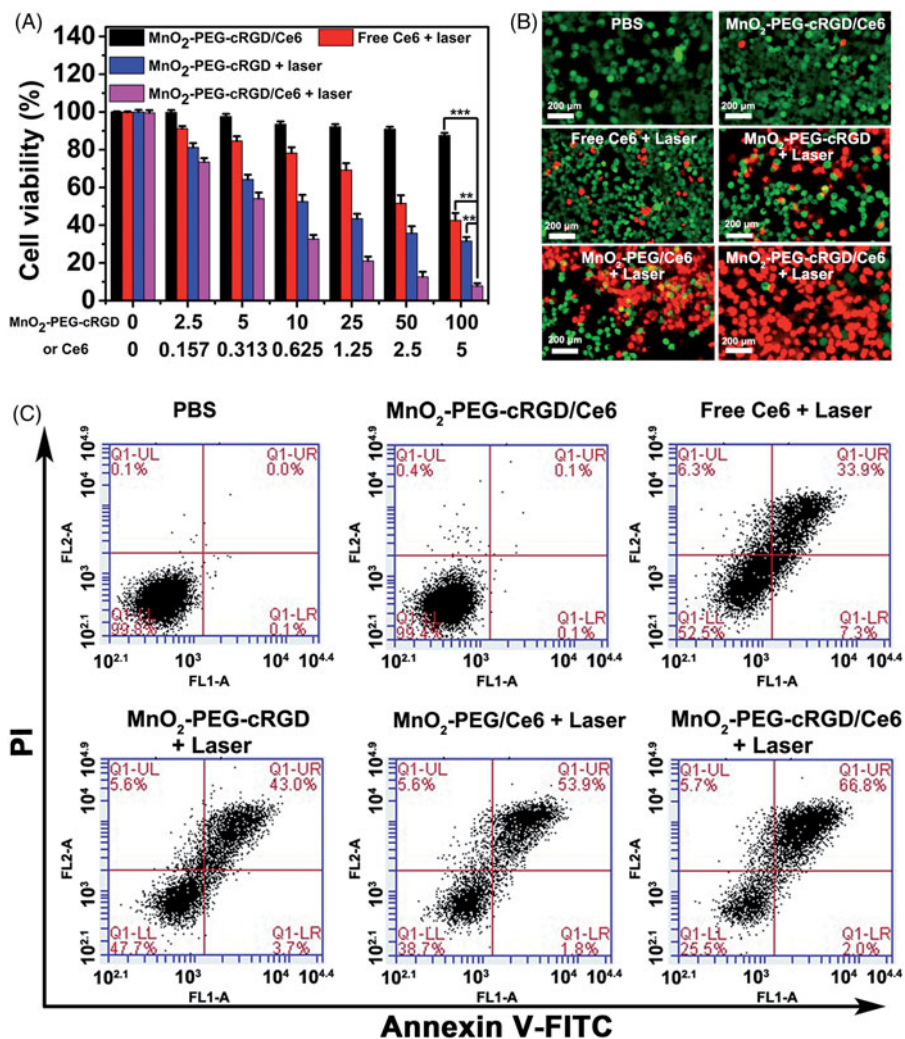


Figure 5. (A) Relative viabilities of PC3 cells after incubation with free Ce6, MnO₂-PEG-cRGD with 660 nm light irradiation or MnO₂-PEG-cRGD/Ce6 with or without 660 nm light irradiation (0.6 W cm⁻², 10 min). ****p* < .001, ***p* < .01. (B) Fluorescence images of calcein-AM (green)/PI (red) double stained cells after different treatments. (C) Flow cytometric analysis of cell apoptosis for 24 h caused by different treatments, using the Annexin V-FITC/PI staining. The four areas represent different phases of the cells: necrotic (Q1), late-stage apoptotic (Q2), early apoptotic (Q3), and live (Q4).

Cell apoptosis assay

To further evaluate the mechanism of synergistic PTT/PDT anticancer effect of PC3 cells, the cells after different treatments were double-labeled with Annexin V-FITC/PI for flow cytometry analysis (Figure 5(C)). As expected, the percentage of apoptosis/necrotic cells was determined to be 68.8% (early apoptosis + later apoptosis) in group of MnO₂-PEG-cRGD/Ce6 with laser irradiation. However, few cells were in apoptosis/necrotic status by the treatment of MnO₂-PEG/Ce6 under laser irradiation (55.7%), as well as compared to the cells after other treatment groups, further indicating the powerful apoptosis-inducing capacity of MnO₂-PEG-cRGD/Ce6 against PC3 tumor cells. These results, together with the MTT result and live/dead staining assay evidenced that the as-fabricated MnO₂-PEG-cRGD/Ce6 simultaneously possess optimal synergistic activity of PDT and PTT.

Compared with previously reported inorganic photothermal agents, the developed MnO₂-PEG-cRGD/Ce6 are especially attractive due to the unique multicomponent functional elements. The photothermal-conversion efficiency

of the prepared nanosheets in this work was calculated to be 37.2%, which is comparable to MnO₂ nanosheets (Liu et al., 2018b; Wu et al., 2018c), Au nanorods (21%; Zeng et al., 2013), Ag₂S (22%; Yang et al., 2017a) and MoS₂-PEG nanoflakes (25.7%) (Feng et al., 2015). On the other hand, compared with previously reported 2D nanosheets-based nanosystems (Ma et al., 2017; Liu et al., 2018b; Ji et al., 2018), the cRGD modification make it can be recognized and taken up by PC3 cells via the receptor-mediated endocytosis mechanism, resulting in enhanced tumor penetration and potent antitumor effect. Also, our work presents a novel multifunctional drug delivery system that is purely composed by biocompatible (PEG) and biodegradable (MnO₂) components, with substantial potential for future clinical translation.

Conclusion

In summary, MnO₂-PEG-cRGD nanosheets loaded with a Ce6 photosensitizer have been successfully prepared and used as a biocompatible nanoplatform for PTT/PDT synergistic cancer

therapy. MnO₂-PEG-cRGD/Ce6 exhibited strong NIR absorption and efficient generation of hyperthermia upon laser irradiation with a high photothermal conversion efficiency of 39%, which is compared to MnO₂-PEG-cRGD nanosheets (28.7%) due to the synergetic effect of MnO₂-PEG-cRGD and Ce6. The introduced cRGD renders nanoplatform with the passive targeting capability. The MnO₂-PEG-cRGD/Ce6 exhibited pH-controlled and NIR-induced Ce6 release. Furthermore, the MnO₂ sheets will be reduced by overexpressed acidic H₂O₂, which could efficiently generate O₂ and further enhancing the therapeutic efficiency of PDT. With the cRGD-mediated targeting ability, MnO₂-PEG-cRGD/Ce6 shows satisfactory antitumor efficacy, which mainly attribute to the combined photothermal and photodynamic outcomes. Moreover, our MnO₂-PEG-cRGD/Ce6 nanosheets may indeed be a promising nanoplatform with great potential for future clinical translation. Also, the photosensitizer loaded strategy in this work also shows general potential for controlled delivery of other biomolecules or drugs to achieve different functions.

Disclosure statement

The author reports no conflicts of interest in this work.

Funding

This work was supported by the Science and Technology Planning Project of Guangdong Province (2014A020212519) and the Key Medical Discipline Construction Project of Guangdong Province.

References

- Bray F, Ferlay J, Siegel RL, et al. (2018). Global cancer statistics 2018: GLOBOCAN estimates of incidence and mortality worldwide for 36 cancers in 185 countries. *CA Cancer J Clin* 68:394–424.
- Chen Q, Feng L, Liu J, et al. (2016a). Intelligent albumin-MnO₂ nanoparticles as pH/H₂O₂-responsive dissociable nanocarriers to modulate tumor hypoxia for effective combination therapy. *Adv Mater* 28: 7129–36.
- Chen L, Feng Y, Zhou X, et al. (2017a). One-pot synthesis of MoS₂ nanoflakes with desirable degradability for photothermal cancer therapy. *ACS Appl Mater Interfaces* 9:17347–58.
- Chen J, Meng H, Yang R, et al. (2019). Recent advances in functionalized MnO₂ nanosheets for biosensing and biomedicine applications. *Nanoscale Horiz* 4:321–38.
- Chen W, Ouyang J, Liu H, et al. (2017b). Black phosphorus nanosheet-based drug delivery system for synergistic photodynamic/photothermal/chemotherapy of cancer. *Adv Mater* 29:1603864.
- Chen Y, Su Y, Hu S, Chen S. (2016b). Functionalized graphene nanocomposites for enhancing photothermal therapy in tumor treatment. *Adv Drug Deliv Rev* 105:190–204.
- Chen Y, Ye D, Wu M, et al. (2014). Break-up of two-dimensional MnO₂ nanosheets promotes ultrasensitive pH-triggered theranostics of cancer. *Adv Mater Weinheim* 26:7019.
- Dai Y, Xu C, Sun X, Chen X. (2017). Nanoparticle design strategies for enhanced anticancer therapy by exploiting the tumour microenvironment. *Chem Soc Rev* 46:3830–52.
- Devaraj S, Munichandraiah N. (2008). Effect of crystallographic structure of MnO₂ on its electrochemical capacitance properties. *J Phys Chem C* 112:4406–17.
- Dong Z, Feng L, Zhu W, et al. (2016). CaCO₃ nanoparticles as an ultrasensitive tumor-pH-responsive nanoplatform enabling real-time drug release monitoring and cancer combination therapy. *Biomaterials* 110: 60–70.
- Fan W, Yung B, Huang P, Chen X. (2017). Nanotechnology for multimodal synergistic cancer therapy. *Chem Rev* 117:13566–638.
- Fang Y, Jiang Y, Zou Y, et al. (2017). Targeted glioma chemotherapy by cyclic RGD peptide-functionalized reversibly core-crosslinked multifunctional poly(ethylene glycol)-b-poly(ϵ -caprolactone) micelles. *Acta Biomater* 50:396–406.
- Feng W, Chen L, Qin M, et al. (2015). Flower-like PEGylated MoS₂ nanoflakes for near-infrared photothermal cancer therapy. *Sci Rep* 5:17422.
- Huo M, Wang L, Chen Y, Shi J. (2017). Tumor-selective catalytic nanomedicine by nanocatalyst delivery. *Nat Commun* 8:357.
- Jaques D, Maestro LM, Rosal BD, et al. (2014). Nanoparticles for photothermal therapies. *Nanoscale* 6:9494–530.
- Ji X, Kong N, Wang J, et al. (2018). A novel top-down synthesis of ultrathin 2D boron nanosheets for multimodal imaging-guided cancer therapy. *Adv Mater* e1803031.
- Karimi M, Ghasemi A, Zangabad PS, et al. (2016). Smart micro/nanoparticles in stimulus-responsive drug/gene delivery systems. *Chem Soc Rev* 45:1457–501.
- Li M, Zhao A, Dong K, et al. (2015). Chemically exfoliated WS₂ nanosheets efficiently inhibit amyloid β -peptide aggregation and can be used for photothermal treatment of Alzheimer's disease. *Nano Res* 8:3216–27.
- Liu B, Li C, Chen G, et al. (2017a). Synthesis and optimization of MoS₂@Fe₃O₄-ICG/Pt(IV) nanoflowers for MR/IR/PA bioimaging and combined PTT/PDT/chemotherapy triggered by 808 nm laser. *Adv Sci (Weinh)* 4:1600540.
- Liu Y, Ji X, Liu J, et al. (2017b). Tantalum sulfide nanosheets as a theranostic nanoplatform for computed tomography imaging-guided combinatorial chemo-photothermal therapy. *Adv Funct Mater* 27:1703261.
- Liu T, Wang C, Cui W, et al. (2014). Combined photothermal and photodynamic therapy delivered by PEGylated MoS₂ nanosheets. *Nanoscale* 6:11219–25.
- Liu Z, Zhang S, Lin H, et al. (2018b). Theranostic 2D ultrathin MnO₂ nanosheets with fast responsibility to endogenous tumor microenvironment and exogenous NIR irradiation. *Biomaterials* 155:54–63.
- Liu Y, Zhen W, Jin L, et al. (2018a). All-in-one theranostic nano agent with enhanced reactive oxygen species generation and modulating tumor microenvironment ability for effective tumor eradication. *ACS Nano* 12:4886–93.
- Lu N, Huang P, Fan W, et al. (2017). Tri-stimuli-responsive biodegradable theranostics for mild hyperthermia enhanced chemotherapy. *Biomaterials* 126:39–48.
- Lucky SS, Soo KC, Zhang Y. (2015). Nanoparticles in photodynamic therapy. *Chem Rev* 115:1990–2042.
- Ma Z, Jia X, Bai J, et al. (2017). MnO₂ gatekeeper: An intelligent and O₂-evolving shell for preventing premature release of high cargo payload core, overcoming tumor hypoxia, and acidic H₂O₂-sensitive MRI. *Adv Funct Mater* 27:1604258.
- Ma N, Zhang MK, Wang XS, et al. (2018). NIR light-triggered degradable MoTe₂ nanosheets for combined photothermal and chemotherapy of cancer. *Adv Funct Mater* 28:1801139.
- Ocoy I, Isiklan N, Cansiz S, et al. (2016). Combined photothermal and photodynamic therapy delivered by PEGylated MoS₂ nanosheets. *Rsc Adv* 6:30285–92.
- Peng L, Mei X, He J, et al. (2018). Monolayer nanosheets with an extremely high drug loading toward controlled delivery and cancer theranostics. *Adv Mater* 30:1707389.
- Shi J, Kantoff PW, Wooster R, Farokhzad OC. (2017). Cancer nanomedicine: progress, challenges and opportunities. *Nat Rev Cancer* 17: 20–37.
- Song X, Liang C, Gong H, et al. (2015). Photosensitizer-conjugated albumin-polyproline nanoparticles for imaging-guided in vivo photodynamic/photothermal therapy. *Small* 11:3932–41.
- Tang H, Zheng Y, Chen Y. (2017). Materials chemistry of nanoultrasonic biomedicine. *Adv Mater* 29:1604105.
- Tian L, Tao L, Li H, et al. (2019). Hollow mesoporous carbon modified with cRGD peptide nanoplatform for targeted drug delivery and

- chemo-photothermal therapy of prostatic carcinoma. *Colloid Surface A* 570:386–95.
- Wu J, Bremner DH, Niu S, et al. (2018a). Chemodrug-gated biodegradable hollow mesoporous organosilica nanotheranostics for multimodal imaging-guided low-temperature photothermal therapy/chemotherapy of cancer. *ACS Appl Mater Interfaces* 10:42115–26.
- Wu J, Bremner DH, Niu S, et al. (2018b). Functionalized MoS₂ nanosheet-capped periodic mesoporous organosilicas as a multifunctional platform for synergistic targeted chemo-photothermal therapy. *Chem Eng J* 342:90–102.
- Wu Y, Li D, Zhou F, et al. (2018c). Versatile in situ synthesis of MnO₂ nanolayers on upconversion nanoparticles and their application in activatable fluorescence and MRI imaging. *Chem Sci* 9:5427–34.
- Xu C, Teng Z, Zhang Y, et al. (2018). Flexible MoS₂-embedded human serum albumin hollow nanocapsules with long circulation times and high targeting ability for efficient tumor ablation. *Adv Funct Mater* 28:1804081.
- Yang Y, Aw J, Xing B. (2017b). Nanostructures for NIR light-controlled therapies. *Nanoscale* 9:3698–718.
- Yang G, Sun X, Liu J, et al. (2016). Light-responsive, singlet-oxygen-triggered on-demand drug release from photosensitizer-doped mesoporous silica nanorods for cancer combination therapy. *Adv Funct Mater* 26:4722–32.
- Yang T, Tang Y, Liu L, et al. (2017a). Size-dependent Ag₂S nanodots for second near-infrared fluorescence/photoacoustics imaging and simultaneous photothermal therapy. *ACS Nano* 11:1848–57.
- Zeng J, Goldfeld D, Xia Y. (2013). A plasmon-assisted optofluidic (PAOF) system for measuring the photothermal conversion efficiencies of gold nanostructures and controlling an electrical switch. *Angew Chem Int Ed* 52:4169–73.
- Zhang W, Guo Z, Huang D, et al. (2011). Synergistic effect of chemo-photothermal therapy using PEGylated graphene oxide. *Biomaterials* 32:8555–61.
- Zhang X, Wu J, Williams GR, et al. (2019). Functionalized MoS₂-nanosheets for targeted drug delivery and chemo-photothermal therapy. *Colloids Surf B Biointerfaces* 173:101–8.
- Zhao Z, Fan H, Zhou G, et al. (2014). Activatable fluorescence/MRI bimodal platform for tumor cell imaging via MnO₂ nanosheet-aptamer nanoprobe. *J Am Chem Soc* 136:11220–3.
- Zhen W, Liu Y, Lin L, et al. (2018). BSA-IrO₂: catalase-like nanoparticles with high photothermal conversion efficiency and a high x-ray absorption coefficient for anti-inflammation and antitumor theranostics. *Angew Chem Int Ed* 57:10309–13.
- Zhong Y, Wang C, Cheng R, et al. (2014). cRGD-directed, NIR-responsive and robust AuNR/PEG-PCL hybrid nanoparticles for targeted chemotherapy of glioblastoma in vivo. *J. Control Release* 195:63–71.